

Flexible RISs: Learning-based Array Manifold Estimation and Phase-shift Optimization

Mohamadreza Delbari¹, Ehsan Mohammadi¹, Mostafa Darabi^{1,2},
Arash Asadi³, Alejandro Jiménez-Sáez¹, and Vahid Jamali¹

¹TU Darmstadt, Germany, ²The University of British Columbia, Canada, ³Delft University of Technology, Netherlands

Abstract—Reconfigurable intelligent surfaces (RISs) are envisioned as a key enabler for next-generation wireless networks, offering programmable control over propagation environments. While extensive research focuses on planar RIS architectures, practical deployments often involve non-planar surfaces, such as structural columns or curved facades, where standard planar beamforming models fail. Moreover, existing analytical solutions for curved RISs are often restricted to specific, pre-defined array manifold geometries. To address this limitation, this paper proposes a novel deep learning (DL) framework for optimizing the phase shifts of non-planar RISs. We first introduce a low-dimensional parametric model to capture arbitrary surface curvature effectively. Based on this, we design a neural network (NN) that utilizes a sparse set of received power measurements to estimate the surface geometry and derive the optimal phase configuration. Simulation results demonstrate that the proposed algorithm converges fast and significantly outperforms conventional planar beamforming designs, validating its robustness against arbitrary surface curvature. We also analyze the impact of the measurement location error on the algorithm’s performance.

I. INTRODUCTION

Reconfigurable intelligent surface (RIS) is a promising technology for next-generation wireless networks, offering programmable control over wireless propagation channels [1]–[3]. To achieve this, RISs must be configured accurately. RISs typically comprise a large number of programmable elements that apply specific phase shifts to incoming signals to reflect them in a desired direction/location. While most existing literature models RISs as planar surfaces, this idealized assumption may not hold in certain practical settings where RISs may need to be mounted on non-planar surfaces, such as structural columns [4], vehicle bodies [5], [6], or curved building facades [7], [8]. To address this challenge, *flexible RISs* are proposed and successfully implemented in [7], [8]. However, if an RIS is implemented on a non-planar surface but its phase shifts are optimized based on a planar assumption, system

The work of M. Delbari, and V. Jamali was supported in part by the Deutsche Forschungsgemeinschaft (DFG, German Research Foundation) within the Collaborative Research Center MAKI (SFB 1053, Project-ID 210487104), in part by the LOEWE initiative (Hesse, Germany) within the emergenCITY Centre under Grant LOEWE/1/12/519/03/05.001(0016)/72, and in part by the German Federal Ministry for Research, Technology and Space (BMFTR) under the program of “Souverän. Digital. Vernetzt.” joint project Open6GHub plus (Project-ID 16KIS2407). Jiménez-Sáez’s work was supported by the Deutsche Forschungsgemeinschaft (DFG, German Research Foundation) – Project-ID 287022738 – TRR 196 MARIE within project C09. Asadi’s work was in part supported by DFG HyRIS (455077022) and DFG mmCell (416765679).

performance, e.g., in terms of data rate, sensing accuracy, or tracking capability, significantly degrades due to the geometric mismatch. Under these conditions, conventional theoretical phase shift optimization may be inefficient.

Although some studies have considered curved RISs and optimized phase shifts analytically, they are typically limited to specific structural geometries [9], [10]. It is also important to distinguish the scope of this work from *flexible and movable RIS* architectures discussed in [11]–[13]. While those studies assume that any individual RIS element locations are known and controllable in addition to their phase shifts, we consider scenarios where the RIS is conformal to a static surface. In our model, element positions are constrained by the underlying geometry and are treated as fixed but unknown variables. This geometry estimation can be formulated as a non-linear, non-convex optimization problem. However, solving this problem iteratively via numerical methods during real-time implementation is computationally prohibitive. Deep learning (DL) methods have received significant attention for wireless communication tasks, offering lower real-time computational complexity and the ability to solve problems that are analytically intractable [14], [15]. For example, [16] optimized RIS phase shifts under partial channel state information (CSI) availability, and [17] exploited DL for RIS near-field (NF) localization. Therefore, in this paper, we develop a neural network (NN)-based method to enable real-time optimization of RIS phase shifts on non-planar surfaces with unknown array manifold geometry.

In this work, we train an NN to implicitly predict the surface geometry and optimize the phase shifts. The input to our NN consists of power measurements taken at various locations when conventional beamforming methods are applied to the surface. To the best of the authors’ knowledge, non-planar RIS phase shift optimization using NNs has not yet been investigated in the literature. Our key contributions are as follows:

- First, we introduce a general parametric model to capture the curvature behavior of the RIS, effectively reducing the dimensionality of the problem from the total number of RIS elements to a smaller subset of variables.
- Next, based on this model, we propose a DL method that, by sampling received power at different mobile user (MU) locations, first estimates the geometry of the curved RIS and subsequently optimizes its phase shifts.
- Finally, we evaluate the performance of the proposed

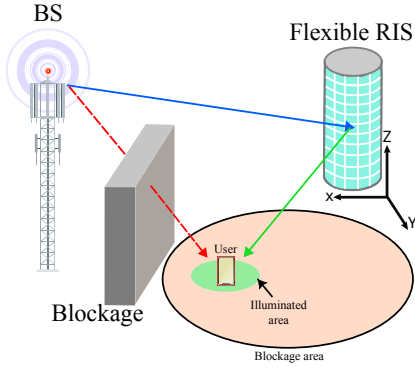


Fig. 1: Schematic illustration of the considered RIS-assisted downlink communication system.

method against benchmarks. We discuss the convergence behavior of the employed NN and compare its performance with a planar design as the variance of the element locations increases. We also show how much the NN is robust against the location error.

Notation: Bold capital and small letters are used to denote matrices and vectors, respectively. $(\cdot)^T$, $(\cdot)^H$, and $\mathcal{U}(a, b)$ denote the Transpose, Hermitian, and Uniform distribution from a to b , respectively. Furthermore, $[\mathbf{A}]_{m,n}$ and $[\mathbf{a}]_n$ denote the element in the m th row and n th column of matrix \mathbf{A} and the n th entry of vector \mathbf{a} , respectively. \mathbb{R} and \mathbb{C} represent the sets of real and complex numbers, respectively. Finally, j is the imaginary unit, and $\mathbb{E}\{\cdot\}$ represents expectation, and $\mathcal{CN}(\mu, \Sigma)$ denotes a complex Gaussian random vector with mean vector μ and covariance matrix Σ .

II. SYSTEM, CHANNEL AND RIS MODEL

In this section, we first introduce the considered system model for K MUs. Subsequently, we describe the channel model along with the considered RIS model.

A. System Model

In this paper, we study a narrow-band downlink communication scenario consisting of a base station (BS) equipped with N_t transmit antennas, an RIS with N unit cells, and K single-antenna MUs (or equivalently K different locations of the same MU). The k th received signal, $y_k \in \mathbb{C}$ is given by:

$$y_k = (\mathbf{h}_{d,k}^H + \mathbf{h}_{r,k}^H \mathbf{\Gamma} \mathbf{H}_t) \mathbf{x} + n_k, \quad (1)$$

where $\mathbf{x} \in \mathbb{C}^{N_t}$ denotes the transmit signal vector, and $n_k \in \mathbb{C}$ is the additive white Gaussian noise (AWGN) at the k th MU, i.e., $n_k \sim \mathcal{CN}(0, \sigma_n^2)$, where σ_n^2 is the noise power. Assuming a linear beamforming, we can write the transmit vector $\mathbf{x} = \mathbf{q}s$, where $\mathbf{q} \in \mathbb{C}^{N_t}$ is the beamforming vector and $s \in \mathbb{C}$ is the data symbol. Here, $\mathbb{E}\{|s|^2\} = 1$ holds so $\|\mathbf{q}\|^2 \leq P_t$ must hold to satisfy the transmit power constraint as P_t denotes the maximum transmit power. Additionally, $\mathbf{h}_{d,k} \in \mathbb{C}^{N_t}$, $\mathbf{H}_t \in \mathbb{C}^{N \times N_t}$, and $\mathbf{h}_{r,k} \in \mathbb{C}^N$ represent the BS-MU, BS-RIS, and RIS-MU channel matrices, respectively. Moreover, $\mathbf{\Gamma} \in \mathbb{C}^{N \times N}$ is a diagonal matrix whose n th diagonal entry is given by $[\mathbf{\Gamma}]_n = [\Omega]_n e^{j[\omega]_n}$, where $[\omega]_n$ and $[\Omega]_n$ correspond to the phase shift and reflection amplitude applied by the n th RIS unit cell. Throughout this paper, we assume $[\Omega]_n = 1$, $\forall n$.

B. Channel Model

Due to the assumption of an extremely large RIS, the distances between the RIS and both the BS and MUs may fall within the NF region of the RIS [18], [19]. Consequently, an NF channel model is adopted. Additionally, since RISs are typically implemented at elevated positions, they maintain line of sight (LOS) links with both the BS and MUs. At high frequencies, these LOS links become even more dominant compared to non-LOS (NLOS) components. Therefore, the channels are modeled using Rician fading with a high K -factor, highlighting the strong contribution of LOS components relative to NLOS components. For generality, we define the channel model in terms of $\mathbf{H} \in \mathbb{C}^{N_{rx} \times N_{tx}}$, where N_{tx} and N_{rx} denote the number of transmitter (Tx) and receiver (Rx) antennas, respectively. A Rician multiple-input multiple-output (MIMO) channel model is written as

$$\mathbf{H} = \sqrt{\frac{K_f}{K_f + 1}} \mathbf{H}^{\text{LOS}} + \sqrt{\frac{1}{K_f + 1}} \mathbf{H}^{\text{NLOS}}, \quad (2)$$

where K_f , \mathbf{H}^{LOS} , and \mathbf{H}^{NLOS} denote the K -factor, LOS, and NLOS NF channels, respectively. K_f determines the power ratio of the LOS component to the NLOS components of the channel. \mathbf{H}^{LOS} and \mathbf{H}^{NLOS} are given by:

$$[\mathbf{H}^{\text{LOS}}]_{m,n} = c_0 e^{j\kappa \|\mathbf{u}_{rx,m} - \mathbf{u}_{tx,n}\|}, \quad (3)$$

$$\mathbf{H}_s^{\text{NLOS}} = c_s \mathbf{a}_{rx}(\mathbf{u}_s) \mathbf{a}_{tx}^T(\mathbf{u}_s), \quad (4)$$

$$[\mathbf{a}_{tx}(\mathbf{u}_s)]_n = e^{j\kappa \|\mathbf{u}_{tx,n} - \mathbf{u}_s\|} \text{ and } [\mathbf{a}_{rx}(\mathbf{u}_s)]_m = e^{j\kappa \|\mathbf{u}_{rx,m} - \mathbf{u}_s\|}, \quad (5)$$

where c_0 denotes the amplitude of the LOS path and $\kappa = \frac{2\pi}{\lambda}$ is the wave number, where λ is wavelength. The variables $\mathbf{u}_{tx,n}$ and $\mathbf{u}_{rx,m}$ correspond to the locations of the n th Tx antenna and the m th Rx antenna, respectively. The steering vectors $\mathbf{a}_{tx}(\cdot) \in \mathbb{C}^{N_{tx}}$ and $\mathbf{a}_{rx}(\cdot) \in \mathbb{C}^{N_{rx}}$ represent the Tx and Rx NF array responses, respectively. Furthermore, \mathbf{u}_s indicates the location of the s th scatterer, and c_s represents the end-to-end amplitude of the s th non-LOS path. Moreover, we assume direct link between BS and MU is blocked, i.e., $\mathbf{h}_{d,k} \approx 0$, $\forall k$.

C. RIS Element Location Model

In this study, we assume the center of the RIS is the center of the global coordinate system. This RIS lies on a non-planar surface extending along the $y - z$ axes. Each RIS element's location can be obtained as $\mathbf{u}_{\text{RIS}}(g) = \mathbf{u}_{\text{RIS}}^\rho + [x, 0, 0]$ where $\mathbf{u}_{\text{RIS}}^\rho = [0, y, z]$, $-\frac{L_y}{2} \leq y \leq \frac{L_y}{2}$, $-\frac{L_z}{2} \leq z \leq \frac{L_z}{2}$ and $x = g(y, z)$ can be defined as a general function. For a planar array, we have $x = g(y, z) = 0$, $\forall (y, z)$, whereas for an arbitrary RIS geometry, $g(y, z)$ is unknown. The spatial placement of the RIS elements is governed by a geometric function, denoted as $x = g(y, z)$. However, exact characterization of the RIS surface geometry is generally an ill-posed problem without prior structural knowledge. To render the problem computationally tractable, we approximate the RIS surface using its Taylor approximation:

$$x = g(y, z) \approx \sum_{m_y=0}^{M_y} \sum_{m_z=0}^{M_{\text{total}}-M_y} a_{m_y, m_z} y^{m_y} z^{m_z}, \quad (6)$$

where $0 \leq M_y \leq M_{\text{total}}$. This parametric approach significantly reduces the dimensionality of the estimation problem from N (all element coordinates) to just the polynomial coefficients ($\frac{(M_{\text{total}}+1)(M_{\text{total}}+2)}{2}$). In this study, a second-order Taylor series approximation ($M_{\text{total}} = 2$) is sufficient to capture common structural curvatures such as cylindrical columns or parabolic facades, but (6) can be used for any M_{total} . By assuming $M_{\text{total}} = 2$, and omitting the constant part, we have a quadratic function of y and z . This models the x -coordinate (depth) of the surface as:

$$x = g(y, z) \approx a_{yy}y^2 + a_{zz}z^2 + a_{yz}yz + a_{yy} + a_{zz}, \quad (7)$$

where the coefficients a_{yy} , a_{zz} , a_{yz} , a_y , and a_z are fixed but unknown parameters for a given deployment that must be estimated. While the exact function g is unknown in practical scenarios, the physical dimensions (ranges of y and z) are typically known. In the subsequent section, we demonstrate how this geometric model is utilized to configure the RIS phase shifts to satisfy a quality of service requirement for the MUs.

III. PROBLEM FORMULATION AND SOLUTION

To optimally configure the RIS phase shifts, accurate estimation of the surface geometry parameters defined in (7) is a prerequisite. We adopt a data-driven approach, utilizing a sampling dataset composed of MU locations and the corresponding RIS configuration phase shifts. We rely exclusively on the received power measurements rather than complex channel state information. This design choice is motivated by the fact that phase measurements are often unstable and require complex synchronization hardware, whereas power measurements are robust and easily accessible [20]. The noiseless received power via the LOS path is¹

$$P(k, \omega; g) = \left| \alpha_0 \int_{-\frac{L_y}{2}}^{\frac{L_y}{2}} \int_{-\frac{L_z}{2}}^{\frac{L_z}{2}} e^{j\omega(y, z) + j\kappa d_k(y, z; g)} dy dz \right|^2, \quad (8)$$

where $d_k(y, z; g) = \kappa \|\mathbf{u}_{\text{RIS}}(g) - \mathbf{u}_{\text{BS}}\| + \kappa \|\mathbf{u}_{\text{RIS}}(g) - \mathbf{u}_{\text{MU},k}\|$, and α_0 captures the total pathloss. The data collection involves K distinct MU locations. For each location k , the RIS cycles through M different phase configurations, denoted as ω_m for $m = 1, \dots, M$. The BS sends a signal and MU measures the resulting signal power for each combination, $P_{k,m} = |y_k(\omega_m)|^2$. The structure of the simulated collected training dataset is summarized in Table I. The non-linear least

$k \setminus \omega$	ω_1	ω_2	\dots	ω_M
1	$P_{1,1}$	$P_{1,2}$	\dots	$P_{1,M}$
2	$P_{2,1}$	$P_{2,2}$	\dots	$P_{2,M}$
\vdots	\vdots	\vdots	\ddots	\vdots
K	$P_{K,1}$	$P_{K,2}$	\dots	$P_{K,M}$

TABLE I: Received power measurements ($P_{k,m}$) across K user locations and M different RIS phase configurations.

¹In millimeter-wave (mmWave), the impact of NLOS paths relative to the LOS path is negligible, especially when narrow beams are adopted.

squares (NLS) problem is formulated as:

$$\hat{g} = \arg \min_g \sum_{k=1}^K \sum_{m=1}^M \left\| P_{k,m} - P(k, \omega; g) \right\|^2. \quad (9)$$

Solving this optimization problem by NLS directly for every RIS deployment is computationally intensive. To address this, we introduce an NN that incurs a one-time training cost but allows for rapid inference during implementation. Furthermore, the NN architecture is generalized, maintaining a consistent structure even if the underlying function changes. The dataset in Table I is utilized to train an NN regressor. The NN takes the received power vector and user coordinates as input and estimates the five geometric coefficients $\{a_{yy}, a_{zz}, a_{yz}, a_y, a_z\}$. Once these coefficients are estimated, the RIS surface is effectively "known," allowing for the analytical or numerical optimization of phase shifts for any future user location.

A. Data Collection and Measurement Point Spacing

The spatial density of measurement points significantly impacts estimation accuracy. To ensure the measurements provide distinct spatial information, the sampling points must be separated sufficiently. For a large array, the normalized beam pattern can be approximated by a sinc function, $\text{sinc}(x) = \sin(\pi x)/(\pi x)$, whose envelope decays proportional to $1/|x|$. To ensure the received power at a neighboring sample point drops sufficiently, e.g., 10 dB relative to the peak, we utilize the decay property of the sinc envelope. A standard heuristic for this distance is approximated by $d_t \approx \frac{2r}{N_t}$, where r is the distance of the received power location from the RIS and N_t is the number of the RIS elements in axis t , $\forall t = \{y, z\}$. For our simulation setup, we have $N_y = 40$, $N_z = 10$, and a distance of $r = 10$ m. These parameters lead to distances of $\frac{2 \times 10}{40} = 0.5$ m and $\frac{2 \times 10}{10} = 2$ m in y and z directions, respectively. These values are confirmed by Fig. 2.

B. Network Architecture and Training

The data set comprises S independent samples generated via the measurement procedure described in Section III. Each sample pairs an input vector of received powers, $\mathbf{x} \in \mathbb{R}^K$, derived in (8), with a target vector of geometric coefficients, $\mathbf{y} \in \mathbb{R}^5$.

1) *Preprocessing and Data Partitioning*: To ensure numerical stability and efficient convergence, the input power measurements are normalized to the range $[0, 1]$ via min-max scaling. The processed dataset is partitioned into training (80%), validation (10%), and testing (10%) sets.

2) *Architecture and Hyperparameters*: We employ a feed-forward multi-layer perceptron (MLP) to model the non-linear mapping between received power and surface geometry. The network consists of an input layer of dimension K , followed by three fully connected hidden layers containing 128, 64, and 32 neurons, respectively. This tapering structure acts to progressively compress the features relevant for geometry extraction.

Rectified linear unit (ReLU) activation is applied to all hidden layers, while the output layer utilizes a linear activation function

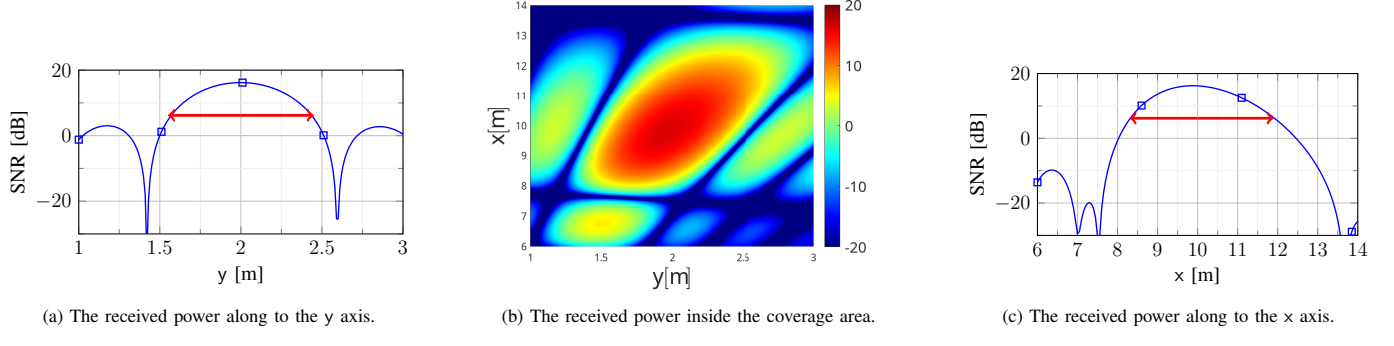


Fig. 2: The required minimum distance for the spatial density of the measurements.

to regress the five continuous parameters of the quadratic surface model discussed in (7). The network is trained using the Adam optimizer to minimize the mean squared error (MSE) loss. Training is set for a maximum of 500 epochs with a mini-batch size of 100. To prevent overfitting, an early stopping mechanism terminates training if the validation loss fails to improve for 50 consecutive epochs.

C. RIS Phase Shift Design

While various techniques exist to optimize RIS phase shifts, $\omega_1, \dots, \omega_M$, our choice is to optimize them such that if RIS would be planar, then all reflected signals add up coherently in the targeted location. Let us assume RIS phase shifts must be optimized for the k' th location, then

$$\omega(y, z) = -\kappa \|\mathbf{u}_{\text{RIS}}^\rho - \mathbf{u}_{\text{BS}}\| - \kappa \|\mathbf{u}_{\text{RIS}}^\rho - \mathbf{u}_{\text{MU}, k'}\|. \quad (10)$$

We substitute (10) into (8) and make our data set for the NN.

IV. PERFORMANCE EVALUATION

A. Simulation Setup

We employ the simulation setup illustrated in Fig. 1. The RIS is centered at the origin of the Cartesian coordinate system, i.e., [0,0,0] m. We assume K different measurement locations inside a fixed area in $\mathcal{P}_u \in \{(x, y, z) : 6 \text{ m} \leq x \leq 14 \text{ m}, 1 \text{ m} \leq y \leq 3 \text{ m}, z = -5\}$. The BS comprises a $4 \times 4 = 16$ uniform planar array (UPA) positioned along the $x - z$ plane, and located at [40, 20, 5] m. The RIS is a uniform non-planar array consisting of $N_y \times N_z = 40 \times 10$ elements aligned to the y and z axes, respectively. The element spacing for both the BS and RIS is half of the wavelength. The noise variance is computed as $\sigma_n^2 = W N_0 N_f$ with $N_0 = -174$ dBm/Hz, $W = 20$ MHz, and $N_f = 6$ dB. We assume 28 GHz carrier frequency, and $\rho(d_0/d)^\sigma$ pathloss model where $\rho = -61$ dB at $d_0 = 1$ m. Moreover, we adopt $S = 18,225$, $K = 25$, $\sigma = (2, 2, 2)$ and $K_f = (0, 10, 10)$ for the BS-MU, BS-RIS, and RIS-MU channels, respectively. The training parameters are given in Table II. Performance was quantified using MSE which is a standard regression metric. This metric was calculated independently for each of the five output parameters to assess the model's predictive accuracy on a per-parameter basis.

TABLE II: Neural Network Hyperparameters

Hyperparameter	Value
<i>Data Partitioning</i>	
Training Set Size	80%
Validation Set Size	10%
Test Set Size	10%
<i>Network Architecture</i>	
Hidden Layers	3 (Dense)
Neuron Configuration	128 \rightarrow 64 \rightarrow 32
Hidden Activation	ReLU
Output Activation	Linear
<i>Training Configuration</i>	
Optimizer	Adam
Learning Rate	0.001
Loss Function	MSE
Maximum Epochs	500
Batch Size	100
Early Stopping Patience	50 Epochs

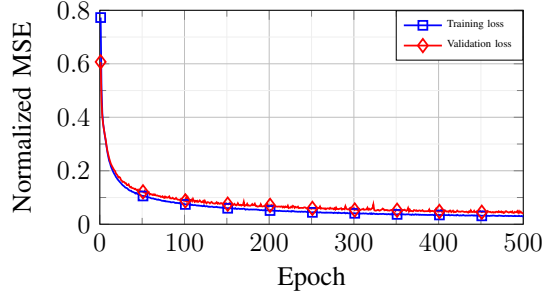


Fig. 3: Training loss and validation loss versus the number of epochs.

B. Simulation Results

First, we study the convergence behavior of the training algorithm in Fig. 3. We plot normalized MSE versus the number of epochs. As the number of epochs increases, the normalized MSE of both the training loss and the validation loss decreases smoothly, confirming convergence.

Fig. 4 shows the Rx signal to noise ratio (SNR) (dB) for different σ values under three different designs. Here, σ is a parameter defining the upper bound of the uniform distribution from which a_{yy} , a_{yz} , and a_{zz} are drawn, i.e., $a_{t_1 t_2} \sim \mathcal{U}(0, \sigma)$, $\forall t_1, t_2 \in \{y, z\}$. Since the RIS geometry is highly sensitive to linear terms (a_y, a_z), these parameters were drawn from a narrower distribution, $\mathcal{U}(-\frac{\sigma}{10}, \frac{\sigma}{10})$. The training data set is optimized for $\sigma = 0.8$. The blue curve

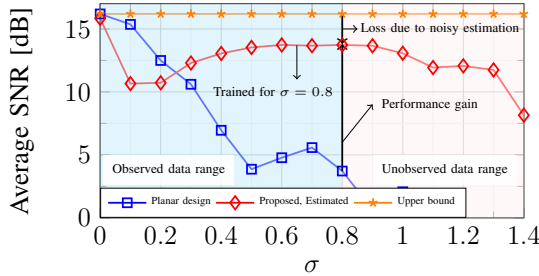


Fig. 4: Rx power at the MU versus the geometric parameter variance.

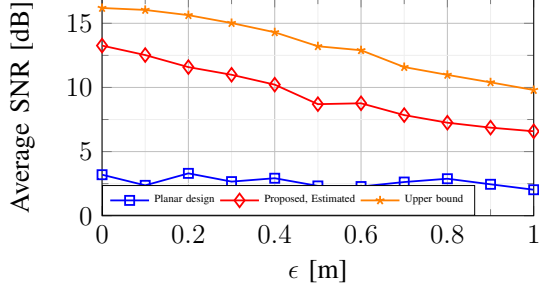


Fig. 5: The Rx power in MU versus the variance of the localization error.

represents the conventional RIS planar model assumption, while the orange curve serves as an upper bound, assuming perfect knowledge of the element locations. Finally, the red curve corresponds to the proposed algorithm. All three methods achieve peak performance at $\sigma = 0$, where the RIS geometry is purely deterministic and planar. In the low-variance regime ($0 < \sigma \leq 0.25$), the planar design remains sufficient and slightly outperforms the proposed algorithm, as the latter is specifically optimized for $\sigma = 0.8$. However, for $\sigma \geq 0.25$, the planar model's performance degrades significantly compared to the proposed design. Notably, the algorithm demonstrates robustness by degrading slowly as σ enters the unobserved data region ($\sigma > 0.8$).

Fig. 5 illustrates the average SNR (dB) at the MU in the presence of location estimation errors. The estimated location of the MU is modeled as $[x + \epsilon_x, y + \epsilon_y, -5]$ m, where both ϵ_x and ϵ_y are drawn from a uniform distribution $\mathcal{U}(-\epsilon, \epsilon)$. As observed, the average SNR decreases as the error increases for both the proposed and the upper bound. Interestingly, the planar design is not significantly affected by location error. This is because, due to the model mismatch, the RIS beam does not point towards the MU in the first place, and further location errors do not significantly affect the received power. The proposed scheme significantly outperforms the planar design even under certain location errors. Utilizing more robust RIS phase-shift designs to mitigate these errors [21] is reserved for future work.

V. CONCLUSION

In this paper, we investigated the problem of beamforming optimization for RISs deployed on non-planar surfaces, a practical scenario where conventional planar assumptions lead to performance degradation. To address the limitations of existing analytical models, which are often restricted to specific geometries, we proposed a robust DL-based framework. We first

developed a parametric model to efficiently represent surface curvature with a reduced number of variables. Subsequently, we designed an NN capable of implicitly estimating the surface geometry and optimizing phase shifts using only sparse Rx power measurements. Simulation results confirmed that the proposed approach not only converges efficiently but also yields performance gains over planar beamforming designs, particularly as the variations in element location increase.

REFERENCES

- [1] Q. Wu and R. Zhang, "Intelligent reflecting surface enhanced wireless network via joint active and passive beamforming," *IEEE Trans. Wireless Commun.*, vol. 18, no. 11, pp. 5394–5409, 2019.
- [2] E. Basar, M. Di Renzo, J. De Rosny, M. Debbah, M.-S. Alouini, and R. Zhang, "Wireless communications through reconfigurable intelligent surfaces," *IEEE Access*, vol. 7, pp. 116 753–116 773, 2019.
- [3] M. Delbari, R. Neuder, A. Jiménez-Sáez, A. Asadi, and V. Jamali, "Fast reconfiguration of liquid crystal-RISs: Modeling and algorithm design," *IEEE Trans. Wireless Commun.*, 2026.
- [4] Y. Chen, Y. Chen, L. Hu, and H. Zhang, "Conformal intelligent reflecting surfaces-assisted networks with reflection constraints," *IEEE Trans. Wireless Commun.*, vol. 24, no. 3, pp. 2265–2278, 2025.
- [5] Tagliaferri *et al.*, "Conformal intelligent reflecting surfaces for 6G V2V communications," in *International Conf. on 6G Netw.*, 2022, pp. 1–8.
- [6] M. Mizmizi *et al.*, "Conformal metasurfaces: A novel solution for vehicular communications," *IEEE Trans. Wireless Commun.*, vol. 22, no. 4, pp. 2804–2817, 2023.
- [7] W.-W. Wang *et al.*, "Flexible liquid crystal micro-lens arrays for curved integral imaging 2D/3D convertible display," *Liquid Crystals*, vol. 50, no. 11-12, pp. 1666–1678, 2023.
- [8] X. He, Y. Cui, and M. M. Tentzeris, "Tile-based massively scalable MIMO and phased arrays for 5G/B5G-enabled smart skins and reconfigurable intelligent surfaces," *Sci. Reports*, vol. 12, no. 1, p. 2741, 2022.
- [9] M. Mizmizi *et al.*, "Conformal metasurfaces: A novel solution for vehicular communications," *IEEE Trans. Wireless Commun.*, vol. 22, no. 4, pp. 2804–2817, 2022.
- [10] P. Mursia *et al.*, "T3DRIS: advancing conformal RIS design through in-depth analysis of mutual coupling effects," *IEEE Trans. Commun.*, vol. 73, no. 2, pp. 889–903, 2025.
- [11] J. An *et al.*, "Flexible intelligent metasurfaces for downlink multiuser MISO communications," *IEEE Trans. Wireless Commun.*, vol. 24, no. 4, pp. 2940–2955, 2025.
- [12] Y. Ren *et al.*, "Flexible-position multi-state RIS-assisted wireless communication: Channel modeling and spatial characteristic measurements," *IEEE J. Sel. Areas in Commun.*, pp. 1–1, 2025.
- [13] K. R. R. Ranasinghe, Z. Wang, G. T. de Abreu, and E. Björnson, "Flexible continuous aperture arrays," *arXiv:2511.09244*, 2025.
- [14] C. Huang, R. Mo, and C. Yuen, "Reconfigurable intelligent surface assisted multiuser MISO systems exploiting deep reinforcement learning," *IEEE J. Sel. Areas in Commun.*, vol. 38, no. 8, pp. 1839–1850, 2020.
- [15] M. A. ElMossallamy *et al.*, "Reconfigurable intelligent surfaces for wireless communications: Principles, challenges, and opportunities," *IEEE Trans. Cogn. Commun. Netw.*, vol. 6, no. 3, pp. 990–1002, 2020.
- [16] B. Peng *et al.*, "RISnet: A domain-knowledge driven neural network architecture for RIS optimization with mutual coupling and partial CSI," *IEEE Trans. Wireless Commun.*, vol. 24, no. 5, pp. 4469–4482, 2025.
- [17] P. Ramezani, S. J. Mousavirad, M. O'Nils, and E. Björnson, "Machine learning-based near-field localization in mixed LoS/NLoS scenarios," *arXiv:2506.17810*, 2025.
- [18] Y. Liu, Z. Wang, J. Xu, C. Ouyang, X. Mu, and R. Schober, "Near-field communications: A tutorial review," *IEEE Open J. of the Commun. Society*, vol. 4, pp. 1999–2049, 2023.
- [19] M. Delbari, G. C. Alexandropoulos, R. Schober, H. V. Poor, and V. Jamali, "Near-field multipath MIMO channel model for imperfect surface reflection," in *Proc. IEEE Globecom*, South Africa, 2024.
- [20] M. Delbari, A. Javaheri, H. Zayyani, and F. Marvasti, "Non-coherent DOA estimation via majorization-minimization using sign information," *IEEE Signal Processing Letters*, vol. 29, pp. 892–896, 2022.
- [21] M. Delbari, G. C. Alexandropoulos, R. Schober, and V. Jamali, "Far-versus near-field RIS modeling and beam design," *arXiv preprint arXiv:2401.08237*, 2024.